

An Ab Initio Study of Monolayer $\text{Mn}_2\text{Mg}_2\text{X}_5$ ($\text{X} = \text{S}, \text{Se}$), a Novel Family of 2D Half-Metallic Ferromagnets

Soheil Ershadrad, Masoumeh Davoudiniya, Nikola Machacova, and Biplab Sanyal*

The recent advances in the synthesis of 2D magnetic materials have raised hopes for their potential use in next-generation spintronics devices. These candidates, however, still possess relatively low magnetic transition temperatures and small magnetic anisotropy energies to achieve efficient functionality. Aiming to find high-performance 2D magnetic crystals, the authors predict $\text{Mn}_2\text{Mg}_2\text{X}_5$ ($\text{X} = \text{S}, \text{Se}$) as a novel family of 2D ferromagnets with half-metallic electronic properties. A single-channel spin bandgap of ≈ 2 eV makes them suitable for spin-filtering applications. Their easy-plane magnetic anisotropy is relatively high, especially in the case of $\text{Mn}_2\text{Mg}_2\text{Se}_5$ ($\text{MAE} = 1.46$ meV/Mn). Furthermore, the magnetic transition temperature of these compounds is relatively high ($T_C \approx 200$ K) compared to those of most synthesized 2D magnetic compounds. The existence of nonmagnetic van der Waals analogs of these compounds, such as $\text{Al}_2\text{Mg}_2\text{Se}_5$, accompanied by their energy, dynamic, thermal, and mechanical stability, suggest that they have a good probability of being synthesized.

anisotropy may stabilize magnetism in thin crystals but some challenges still remain, such as low Curie temperature (T_C) or air sensitivity. Fortunately, between the various families of 2D magnets (i.e. insulating, semiconducting, half-metallic, and metallic), a significant increase in the T_C of metallic systems has recently been achieved. The thin films of metallic Fe_nGeTe_2 (where $n = 3, 4$, and 5) exhibit ferromagnetism, close to room temperature.^[9–11] Moreover, their T_C can be further increased via doping.^[12] Among them, only Fe_3GeTe_2 is exfoliated up to 2D regime.^[13] However, other 2D magnet families, including half-metallic systems, have been less explored, and despite many predictions, no candidate has yet been found that is functional at room temperature.


1. Introduction

In the context of an isotropic spin Hamiltonian, Mermin–Wagner theorem^[1] states that thermal spin fluctuations prevent 2D materials from developing long-range magnetic order at a finite temperature. However, if magnetic anisotropy is present, this restriction is lifted, allowing 2D magnets to be realized. Similar to the first 2D materials, the first attempts to obtain 2D magnetic materials were by exfoliation of layered magnetic materials.^[2,3] However, reducing the dimensionality of a material may give rise to new properties—change of magnetic ordering temperature with respect to the number of layers is often observed. Despite several theoretical predictions,^[4–6] (ferro) magnetism in 2D materials had not been experimentally confirmed until 2017 in $\text{Cr}_2\text{Ge}_2\text{Te}_6$ ^[7] and CrI_3 .^[8] Magnetic

Half-metals were first introduced by de Groot et al.^[14] to describe the calculated electronic structure of Mn-based Heusler alloys. Similar properties were also suggested for surface,^[15] which opened the possibility of half-metallicity in 2D materials. The interesting nature of half-metals arises from a different placement of d orbitals for each spin, which makes the material conductive in majority spin and insulating in minority spin. Most half-metals have ferromagnetic (FM) ordering, even though few antiferromagnetic (AFM) materials have been predicted as well, e.g., perovskite oxides.^[16,17] Half-metallicity can also be induced via doping^[18–20] or defect engineering.^[21] In the 2D regime, half-metallic magnets are expected to have higher transition temperatures compared to their semiconductor counterparts. This is mainly due to the higher concentration of charge carriers in these systems, which strengthens the exchange interactions among magnetic atoms. Although there have been several reports of induced half-metallicity in 2D systems, via doping, intrinsic 2D half-metallic magnets are rarely reported. Recently, Wang et al.^[22] have predicted MnX ($\text{X} = \text{P}, \text{As}$) monolayers, as 2D half-metallic systems with high T_C . Also Janus Mn_2 PAs monolayer and NiOX ($\text{X} = \text{Cl}, \text{Br}$) were proposed as 2D half-metals with high T_C .^[23,24]

The family of van der Waals $\text{X}_2\text{Y}_2\text{Z}_5$ (X and Y are metallic atoms and Z is a group VI element) have some already synthesized members, that are analogous to the structures, studied in this article. Among them, we can refer to $\text{Al}_2\text{Mg}_2\text{Se}_5$,^[25,26] $\text{Bi}_2\text{Pb}_2\text{Se}_5$,^[26–28] $\text{Pb}_2\text{Sb}_2\text{Te}_5$,^[28] and $\text{Fe}_2\text{Ga}_2\text{S}_5$.^[29,30] The magnetic members of this family are often found to have an AFM ground state. Shen et al.^[31] have recently reported the synthesis of single crystals of $\text{Mn}_2\text{Ga}_2\text{S}_5$. Their findings revealed substantial AFM interactions, and a high spin state in Mn^{2+} ions.

S. Ershadrad, M. Davoudiniya, N. Machacova, B. Sanyal
Department of Physics and Astronomy
Uppsala University
Box-516, SE 75120 Uppsala, Sweden
E-mail: biplab.sanyal@physics.uu.se

 The ORCID identification number(s) for the author(s) of this article can be found under <https://doi.org/10.1002/pssb.202300496>.

© 2023 The Authors. physica status solidi (b) basic solid state physics published by Wiley-VCH GmbH. This is an open access article under the terms of the Creative Commons Attribution-NonCommercial License, which permits use, distribution and reproduction in any medium, provided the original work is properly cited and is not used for commercial purposes.

DOI: 10.1002/pssb.202300496

Remarkably, it undergoes a spin-freezing transition at around 12 K, illustrating a highly frustrated system characterized by the absence of long-range magnetic order down to 2 K. This behavior arises from the intricate interplay between exchange interactions and the material's 2D crystalline structure. In this family, however, no FM-ordered system has been reported.

The present work examines the structural, mechanical, electronic, and magnetic properties of $\text{Mn}_2\text{Mg}_2\text{X}_5$ monolayers using ab initio methods. Following is a brief summary of the article:

In Section 2, a detailed description of the computational methodology can be found. In Section 3, we report the structural properties of these compounds. In Section 4, first, the cohesive and formation energies are used to determine the energetic stability. After that, dynamical, thermal, and mechanical stability are examined. The next step is the study of the magnetic (Section 5), mechanical (Section 6), and electronic properties (Section 7) of $\text{Mn}_2\text{Mg}_2\text{X}_5$ monolayers, as well as the modeling of temperature-dependent magnetic properties through Monte Carlo (MC) simulations (Section 8). The final section of this article concludes our results.

2. Methodology

First-principles calculations were conducted in the framework of density-functional theory (DFT)^[32,33] using the Vienna ab initio simulation package (VASP).^[34–37] The exchange–correlation potential was treated using the generalized gradient approximation functional in conjunction with the Perdew, Burke, and Ernzerhof method.^[38] The projector augmented wave method^[39] was applied. We utilized the DFT+U method to improve the description of strongly correlated d-electrons in Mn atoms, with U_{eff} set to 3 eV, in accordance with Hubbard corrections suggested for Mn-containing compounds.^[40–42] Furthermore, the consistency of the results was examined by varying U_{eff} values between 2 and 4 eV (see Figure S8 for $U = 2$ eV and Figure S9 for $U = 4$ eV in Supporting Information). A plane-wave basis set with a kinetic cutoff energy of 500 eV was used to expand the

electronic wave function, and a vacuum space of at least 15 Å was inserted along c – axis to prevent unrealistic interactions between periodic images. During structural optimization, the maximum force on each atom was less than $10^{-2} \text{ eV Å}^{-1}$. A Gaussian smearing factor of 0.05 was taken into account. Brillouin zone (BZ) integration was performed by a Γ -centered $17 \times 17 \times 1$ uniform k -point grid. To determine the net charge transfer between constituent atoms, the Bader technique was employed.^[43] To ensure the dynamical stability of the systems, the phonon dispersions were calculated, using the finite-displacement approach, implemented in the PHONOPY^[44] package. To analyze the thermal stability, ab initio molecular dynamics (AIMD) simulations were conducted, using a microcanonical ensemble (NVE), at constant temperatures of $T = 300$ and 500 K for a simulation period of 10 ps with a 2 fs time step. A $4 \times 4 \times 1$ supercell and a $4 \times 4 \times 1$ k -point grid were used for phonon dispersions, AIMD, and calculations of mechanical properties. For the calculation of magnetic anisotropy energy (MAE), a $31 \times 31 \times 1$ k -point grid was utilized. For the MAE calculations, spin–orbit coupling (SOC) was taken into account. The projection into localized Wannier functions (WFs) was carried out using the Wannier90 package,^[45] via VASP to Wannier90 interface. The WFs basis set comprised five d orbitals of Mn atoms and three p-orbitals of X (X = S, Se) atoms. The TB2J^[46] package was utilized to calculate isotropic exchange interactions via Liechtenstein, Katsnelson, Antropov, and Gubanov^[47] formalism. The extracted exchange interactions were implemented in a Heisenberg Hamiltonian to calculate the magnetic ordering temperature by performing classical MC simulations via UppASD code.^[48] To achieve properly averaged properties, three ensembles within a supercell of $40 \times 40 \times 1$ were modeled, assuming periodic boundary conditions.

3. Structural Analysis

The $\text{Mn}_2\text{Mg}_2\text{X}_5$ (X = S, Se) monolayer is demonstrated from both side and top views, as illustrated in **Figure 1a,b**, respectively.

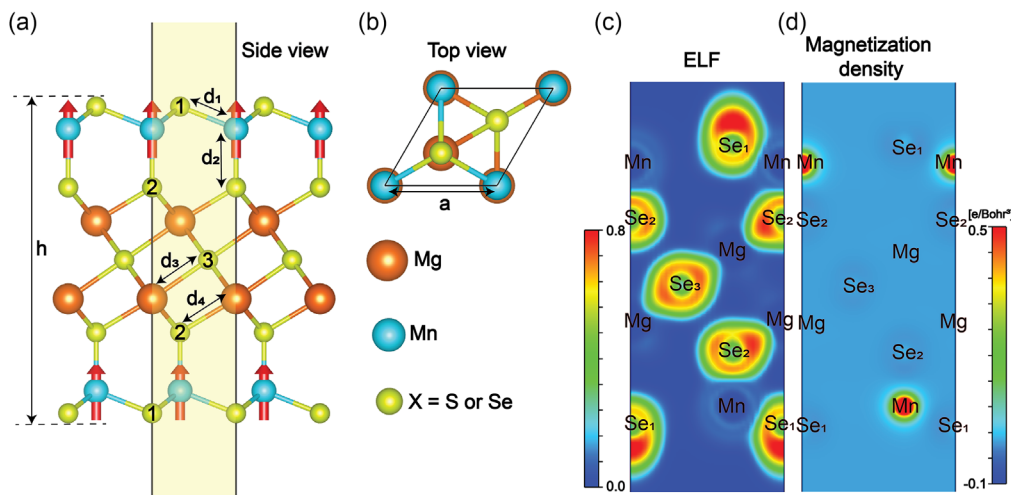


Figure 1. a) Side and b) top views of the $\text{Mn}_2\text{Mg}_2\text{X}_5$ monolayers, c) electron-localization function iso-surface on $(\bar{1}, 1, 0, 0)$ plane, and d) magnetization density iso-surface on $(\bar{1}, 1, 0, 0)$ plane in $\text{Mn}_2\text{Mg}_2\text{Se}_5$. Double-headed arrows display the geometrical parameters. The yellow shaded area represents the unit cell.

It is classified based on the element type and coordination number, highlighting the presence of five distinct atomic sites. For ease of referencing, we have labeled X atoms with numbers from 1 to 3 in Figure 1a, for three-, four-, and sixfold coordination sites, respectively. Both structures belong to space group symmetry P-3m1 (number 164). From a lateral perspective, the structure appears to have a trilayered arrangement, where the central layer consists of Mg and X atoms, positioned between two layers comprising Mn and X species. Within this central layer, Mg atoms create six bonds with neighboring X atoms, while in the top and bottom, Mn atoms are fourfold coordinated. The structural thickness, symbolized as h , is defined as the vertical separation between the topmost and lowest chalcogen atoms. We have also identified atomic bond lengths, i.e., Mg-X₁, Mg-X₂, Mg-X₃, and Mg-X₄, using d_1 , d_2 , d_3 , and d_4 , respectively. The structural parameters are detailed in Table 1. In the case of Mn₂Mg₂S₅, the lattice constant is determined to be $a = 3.83$ Å, while we observe a lattice expansion, reaching a value of $a = 3.99$ Å, for Mn₂Mg₂Se₅, as the atomic radius of the group VI elements increases. Similarly, the thickness of the Mn₂Mg₂S₅ monolayer, $h = 11.89$ Å, is observed to be smaller than that of the Mn₂Mg₂Se₅ monolayer, which equals 12.92 Å. The analysis of bond lengths reveals that the bonds in Mn₂Mg₂Se₅ are more extended than Mn₂Mg₂S₅, reflecting Se's larger atomic radius. Between the Mn-X bonds, d_4 is shorter than d_3 and between the Mg-X bonds, d_2 is shorter than d_1 , which supports the correlation between bond length and coordination number. In other words, longer bonds occur when the charge is spread among a greater number of bonds.

The Bader charge analysis results are listed in Figure S1 (Supporting Information). It can be noted that Mn and Mg atoms are charge donors and chalcogen atoms are charge acceptors. In both compounds, Mn atoms lose a charge of more than 1e. Moreover, by losing over 1.5e of their charge, Mg atoms are somewhere between Mg⁺ and Mg²⁺ states. To have a charge balance, $\approx 5e$ charge donated by Mn and Mg atoms is distributed between five chalcogens of the unit cell. Although almost 1e charge is accepted by each S (Se) atom, the crystal symmetry and coordinating numbers dictate an uneven distribution of charge between chalcogen atoms. Accordingly, the S₃ (Se₃) atoms at the central region along c axis gain maximum charge while S₁ (Se₁) atoms at the surfaces receive the minimum charge, and S₂ (Se₂) sites accept a charge close to that of nominal 1e.

In Figure 1c, isosurface of the electron-localization function along the $(\bar{1}, 1, 0, 0)$ plane of the Mn₂Mg₂Se₅ monolayer is plotted (see Figure S2, Supporting Information, for that of Mn₂Mg₂S₅). Here, red contours indicate a higher probability

Table 1. The structural, energetic, and electronic nature of the Mn₂Mg₂X₅ compounds, where a is the lattice parameter, h is the thickness of the monolayer, $d_{(1-4)}$ are bond lengths in unit of Å, E_{coh} and E_{form} are the cohesive and formation energies in unit of eV atom⁻¹, respectively, and "Type" specifies the electronic nature.

Structure	a	h	d_1	d_2	d_3	d_4	E_{coh}	E_{form}	Type
Mg ₂ Mn ₂ S ₅	3.83	11.89	2.37	2.30	2.68	2.55	3.94	-0.84	Half-metal
Mg ₂ Mn ₂ Se ₅	3.99	12.92	2.51	2.46	2.82	2.67	3.48	-0.72	Half-metal

of electron localization relative to a reference electron,^[49] which provides information about the bonding nature of these compounds. Remarkably, we observe a significant electron localization around the chalcogen sites, evidence of covalent bonds between Mn(Mg) and chalcogen atoms.

The contour plot of magnetization density within a $(\bar{1}, 1, 0, 0)$ plane of the single-layer Mn₂Mg₂Se₅ is presented in Figure 1d. It can be noted that the magnetization density primarily originates from Mn atoms. Nevertheless, there are some small induced moments on chalcogen sites, which are opposite to those on Mn atoms. In addition, Mg atoms do not show any sign of magnetization.

4. Stability

4.1. Energetic Stability

Synthesizability of new materials is first dependent on their energetic stability. The cohesive energy (E_{coh}) is a measure of how much energy is required to disassemble a crystallized system into detached atoms, and its magnitude is a measure of how strongly the atoms are bound together. In contrast, a compound's formation energy (E_{form}) is the difference between its total energy and the energy of the most stable bulk form of its constituent elements. Thus, a positive E_{form} indicates that a compound tends to decompose into more stable structures. Hence, it is essential to examine the cohesive and formation energies of our compounds to determine their stability. The following expressions are used to calculate E_{coh} and E_{form} :

$$E_{\text{coh}} = \frac{2E_{\text{Mn}} + 2E_{\text{Mg}} + 5E_{\text{X}} - E_{\text{T}}}{9} \quad (1)$$

$$E_{\text{form}} = \frac{E_{\text{T}} - 2E_{\text{Mn}}^{\text{B}} - 2E_{\text{Mg}}^{\text{B}} - 5E_{\text{X}}^{\text{B}}}{9} \quad (2)$$

where E_{T} is the total energy of the crystalline system; E_{Mn} , E_{Mg} , and E_{X} are the total energies of a single free-standing atom of Mn, Mg, and S(Se) for calculation of cohesive energy, and that of Mn, Mg, and S(Se) atoms in their bulk form for calculation of formation energy. For each element, the most stable bulk form is retrieved from the Materials Project database,^[50] and then reoptimized based on compatible optimization parameters. The obtained values are detailed in Table 1. For Mn₂Mg₂S₅ and Mn₂Mg₂Se₅, E_{coh} of 3.94 and 3.48 eV atom⁻¹ are obtained, respectively, suggestive of strong interatomic bonds. The cohesive energies of these compounds are comparable to those of synthesized phosphorene (3.48 eV atom⁻¹),^[51] silicene (2.58 eV atom⁻¹),^[52] and CrI₃ (2.32 eV atom⁻¹),^[53] implying the synthesizability of these compounds. Furthermore, both monolayers have negative formation energies, another indication of energetic stability, where E_{form} of Mn₂Mg₂S₅ and Mn₂Mg₂Se₅, are obtained to be -0.84 and -0.72 eV atom⁻¹, respectively. This difference in cohesive and formation energies of Mn₂Mg₂S₅ and Mn₂Mg₂Se₅ stems from the greater electronegativity of S atoms. These formation energies are more favorable than that of CrI₃ (-0.18 eV atom⁻¹)^[54] and Fe₃GeTe₂ (-0.08 eV atom⁻¹).^[55]

4.2. Dynamical Stability

Assured of their energetic stability, we further analyzed the dynamical (vibrational) stability of $\text{Mn}_2\text{Mg}_2\text{X}_5$ compounds using their phonon spectra, as depicted in **Figure 2a**. Phonon spectrum analysis confirms the absence of imaginary frequencies, indicating structural stability. In the context of harmonic approximation, imaginary frequencies imply a repulsive interatomic force that makes the structure unstable. In a 3D system, atoms have three degrees of freedom for collective motion along the X, Y, and Z axes. $\text{Mn}_2\text{Mg}_2\text{X}_5$ unit cells consist of 9 atoms, yielding 27 vibrational modes. Unlike conventional 3D crystals where all acoustic modes display linear dispersion near the Γ point, in 2D materials like $\text{Mn}_2\text{Mg}_2\text{X}_5$, the out-of-plane acoustic branch exhibits quadratic dispersion. One can observe the similarities between the two phonon spectra due to similar symmetries. The optical modes in $\text{Mn}_2\text{Mg}_2\text{Se}_5$, however, are collectively shifted to lower frequencies compared with $\text{Mn}_2\text{Mg}_2\text{S}_5$, corresponding to an increase in atomic mass and aligns with a similar pattern in bond strength.

4.3. Thermal Stability

We performed AIMD simulations for a 10 ps duration to investigate the thermal behavior of $\text{Mn}_2\text{Mg}_2\text{X}_5$ monolayers at temperatures of 300 and 500 K. This analysis provided insights into the compound's structural integrity and thermal stability. The energy

variations over the simulation period, as well as the final atomic configuration after 10 ps, at $T = 300$ K are illustrated in **Figure 2b** and at $T = 500$ K in **Figure S3** (Supporting Information). At $T = 300$ K, the energy variations exhibited minor fluctuations, maintaining their proximity to the average values, thus confirming the thermal stability of both structures, when exposed to room temperature. It is evident from the structural snapshots that there are no broken chemical bonds, thereby ensuring the preservation of the overall structural integrity of the $\text{Mn}_2\text{Mg}_2\text{X}_5$ compounds after the simulation. At $T = 500$ K, while $\text{Mn}_2\text{Mg}_2\text{S}_5$ retains minor oscillations in its energy, thermal fluctuations in $\text{Mn}_2\text{Mg}_2\text{Se}_5$ are more drastic, indicative that some bond breaking occurs. The final structural snapshot in $\text{Mn}_2\text{Mg}_2\text{Se}_5$ also reveals displacement of Mn atoms from their equilibrium position, leading to local clustering of Mn atoms. These results suggest that $\text{Mn}_2\text{Mg}_2\text{S}_5$ maintains its thermal stability at 500 K while $\text{Mn}_2\text{Mg}_2\text{Se}_5$ loses its thermal stability close to 500 K.

4.4. Mechanical Stability

Based on the Born and Huang criteria,^[56,57] to have mechanical stability in 2D hexagonal crystals, two conditions should be satisfied, i.e., $C_{11} > |C_{12}|$ and $C_{66} = (C_{11} - C_{12})/2 > 0$, where C_{11} , C_{12} , and C_{66} are the elastic stiffness constants calculated by fitting the second derivative of strain energy per unit area as a function of the in-plane strains. Having the elastic stiffness constants in hand, within the elastic regime, Young's modulus

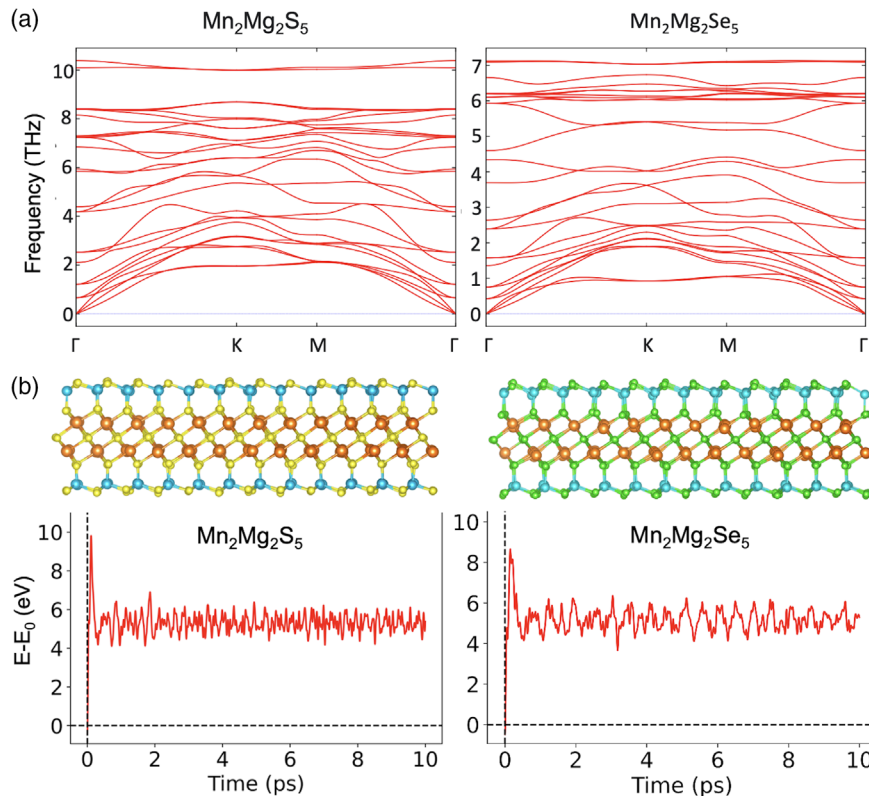


Figure 2. a) Phonon-dispersion spectra and b) ab initio molecular dynamics (AIMD) simulations for $\text{Mn}_2\text{Mg}_2\text{S}_5$ (left panel) and $\text{Mn}_2\text{Mg}_2\text{Se}_5$ (right panel) structures at $T = 300$ K.

Table 2. The elastic constants and mechanical properties of the $\text{Mn}_2\text{Mg}_2\text{X}_5$ compounds, where C_{11} , C_{12} , and C_{66} are components of the elastic constants matrix for 2D hexagonal crystals in units of N m^{-1} , Y_{2D} is Young's modulus in units of N m^{-1} , ν is Poisson's ratio, and the ultimate tensile strain is denoted by UTS in units of %.

Structure	C_{11}	C_{12}	C_{66}	Y_{2D}	ν	UTS
$\text{Mg}_2\text{Mn}_2\text{S}_5$	102.7	36.7	33.0	89.7	0.35	14
$\text{Mg}_2\text{Mn}_2\text{Se}_5$	79.2	27.4	25.9	69.7	0.35	14

($Y_{2D} = (C_{11}^2 - C_{12}^2)/C_{11}$), and Poisson's ratio ($\nu = C_{12}/C_{11}$) can be estimated. The mechanical properties of $\text{Mn}_2\text{Mg}_2\text{X}_5$ compounds are listed in **Table 2**, where C_{11} , C_{12} , and C_{66} are 102.7, 36.7, and 33.0 N m^{-1} , respectively, for $\text{Mg}_2\text{Mn}_2\text{S}_5$ and C_{11} , C_{12} , and C_{66} are 79.2, 27.4, and 25.9 N m^{-1} , respectively, for $\text{Mg}_2\text{Mn}_2\text{Se}_5$. One can note that both structures satisfy the Born and Huang criteria for mechanical stability.

5. Magnetic Properties

Having established the energetic, dynamical, thermal, and mechanical stability of $\text{Mn}_2\text{Mg}_2\text{X}_5$ compounds, we further studied their magnetic behavior. To find the magnetic ground state of these systems, we searched for the minimum energy among FM and several possible AFM arrangements as schematically illustrated in Figure S4 (Supporting Information). It can be noted that in both compounds, FM order is the lowest in energy and thus the ground state. The AFM-1 configuration with intra-sub-layer ferromagnetism and inter-sub-layer antiferromagnetism is the second best configuration energetically with an energy difference of 6.0 and 9.6 meV/Mn with respect to FM arrangement, for $\text{Mn}_2\text{Mg}_2\text{S}_5$ and $\text{Mn}_2\text{Mg}_2\text{Se}_5$, respectively. The configurations with intra-sub-layer antiferromagnetism, i.e., AFM-2 and AFM-3, have a notable energy difference of more than 80 meV/Mn with respect to the FM ground state. Accordingly, all the structural, magnetic, and electronic calculations are performed for the FM ground state.

In the $\text{Mn}_2\text{Mg}_2\text{X}_5$ compounds, a magnetic moment of close to $4 \mu_B$ is stabilized on Mn sites, as listed in **Table 3**. An induced magnetic moment between -0.1 and $-0.2 \mu_B$ can also be observed on the chalcogen sites. **Figure 3** (upper panels) provides information about the Heisenberg exchange interactions (J_{ij}) in $\text{Mn}_2\text{Mg}_2\text{X}_5$ crystals. The strong positive first neighbor intra-sub-layer interaction in both $\text{Mn}_2\text{Mg}_2\text{S}_5$ ($J_{11} = 12.3 \text{ meV}$) and $\text{Mn}_2\text{Mg}_2\text{Se}_5$ ($J_{11} = 10.1 \text{ meV}$) compounds is the driving force behind the overall FM order in these systems. The second intra-sub-layer exchange interaction is AFM. Despite this, these

AFM interactions cannot overcome the strong FM contribution of first neighbors. Third neighbor interactions are FM in both compounds and stronger than those of second neighbors. The intra-sub-layer interactions become negligible after the third neighbor. In these systems, the first neighbor inter-sub-layer exchange interaction (J_{12}) is weakly AFM, contradicting overall ferromagnetism. However, the second neighbor inter-sub-layer exchange interaction is FM and compensates for the first neighbor AFM interaction, rendering the FM ground state. The relatively small energy difference between the FM and AFM-1 configurations (see Figure S4, Supporting Information) stems from the relatively weak coupling between the Mn_1 and Mn_2 species in two magnetic sub-layers. Dictated by the symmetry of the structures, J_{22} interactions are equivalent to that of J_{11} , the same is true of J_{12} and J_{21} , as well.

To have an insight into the exchange mechanism in $\text{Mn}_2\text{Mg}_2\text{X}_5$ monolayers, the orbital decomposition of the strongest exchange interaction (first neighbor J_{11}) is listed in Figure 3 (lower panels), where the dominant interaction is highlighted in red. It can be noted that $d_{z^2} - d_{z^2}$ interactions between the two neighboring Mn atoms (5.41 and 4.05 meV in $\text{Mn}_2\text{Mg}_2\text{S}_5$ and $\text{Mn}_2\text{Mg}_2\text{Se}_5$, respectively) constitute the strongest interaction. Since the d_{z^2} orbitals have out-of-plane orientation while Mn atoms are lying on a xy sub-layer, we predict an indirect exchange mechanism mediated by p_z orbitals of chalcogen atoms. The tight-binding hopping parameters also support this exchange mechanism, where the d_z - p_z -hopping parameter between Mn and Se₂ sites with $t = 1.2$ (1.1) eV for spin-up (down), are at least two orders of magnitude stronger than hopping parameters between various d orbitals of two neighboring Mn atoms ($t < 0.03 \text{ eV}$). Thus, in these monolayers, the primary exchange mechanism is indirect, via nearby chalcogen atoms, giving rise to strong FM interaction.

We further studied the magnetocrystalline anisotropy energy (MAE) in these systems, using magnetic force theorem:

$$\text{MAE} = E_{\perp} - E_{\parallel} \quad (3)$$

where E_{\perp} and E_{\parallel} are the total energies when moments are aligned along out-of-plane and in-plane directions, respectively. Accordingly, both monolayers show easy-plane magnetism (where the anisotropy within the xy plane is negligible). The MAE for $\text{Mn}_2\text{Mg}_2\text{S}_5$ and $\text{Mn}_2\text{Mg}_2\text{Se}_5$ are found to be 0.023 and 1.46 meV/Mn, respectively, as listed in Table 3, where a positive value indicates the easy-plane nature. As a result of the stronger SOC in heavier Se atoms, $\text{Mn}_2\text{Mg}_2\text{Se}_5$ exhibits a higher MAE. A comparison with monolayers of CrI_3 ($\approx -0.80 \text{ meV/Cr}$), CrBr_3 ($\approx -0.16 \text{ meV/Cr}$), $\text{Cr}_2\text{Ge}_2\text{Te}_6$ ($\approx 0.33 \text{ meV/Cr}$), and Fe_3GeTe_2 ($\approx -1.22 \text{ meV/Fe}$)^[11,58,59] shows that $\text{Mn}_2\text{Mg}_2\text{Se}_5$

Table 3. Magnetic properties of $\text{Mn}_2\text{Mg}_2\text{X}_5$ structures, M–Mn and M–X_i are the magnetic moments on Mn and X sites (S, Se), respectively, in units of μ_B , MAE is the magnetic anisotropy energy in units of meV/Mn, where a positive value indicates easy-plane anisotropy, J_1 , J_2 , and J_3 are first, second, and third neighbor isotropic Heisenberg exchange interactions, respectively, in units of meV, $T_{C\text{-MF}}$ and $T_{C\text{-MC}}$ are the mean-field and MC magnetic transition temperatures, respectively, in units of K.

Structure	M–Mn	M–Se ₁	M–Se ₂	M–Se ₃	MAE	J_1	J_2	J_3	$T_{C\text{-MF}}$	$T_{C\text{-MC}}$
$\text{Mg}_2\text{Mn}_2\text{S}_5$	4.18	−0.17	−0.13	−0.09	0.023	12.3	−0.7	1.88	316	205
$\text{Mg}_2\text{Mn}_2\text{Se}_5$	4.29	−0.19	−0.16	−0.13	1.46	10.1	−0.4	1.6	276	193

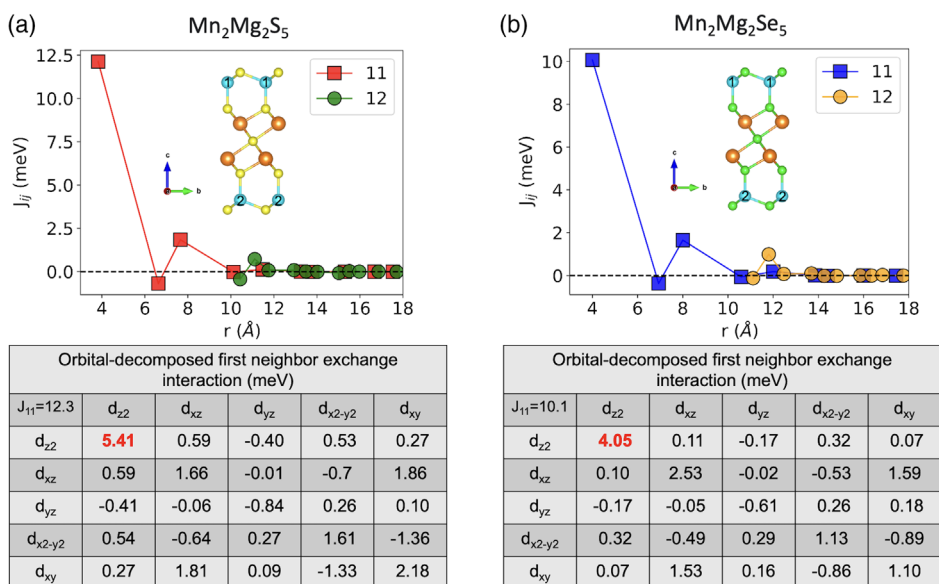


Figure 3. Isotropic Heisenberg exchange interactions (J_{ij}) (upper panel), where J_{11} are interactions between Mn_1 sites and J_{12} are interactions between Mn_1 and Mn_2 sites, and orbital-decomposed first neighbor interaction (J_{11}) (lower panel) for a) $\text{Mn}_2\text{Mg}_2\text{S}_5$ and b) $\text{Mn}_2\text{Mg}_2\text{Se}_5$ structures, where the strongest contribution is highlighted in red.

possess a relatively strong magnetic anisotropy, which is essential for the stabilization of FM order at elevated temperatures and desirable for potential applications in spintronics and magnetic devices. The angular dependence of the MAE can be described using the following expression:

$$\text{MAE} = k \cos^2(\Theta) \quad (4)$$

where k is the anisotropy constant and Θ is the polar angle of rotation. While gradually varying the Θ angle, we fitted this formula to the total energy set (see Figure 4). It can be noted that there is a good match between the fitted curve and the calculated energies, where k has a positive value, indicating the easy-plane nature of anisotropy.

6. Mechanical Properties

Young's modulus is the ratio between stress and strain in a material, and monolayers with a high Y_{2D} require higher stress to

deform elastically. We obtained a Y_{2D} of 89.7 N m^{-1} for $\text{Mn}_2\text{Mg}_2\text{S}_5$ and 69.7 N m^{-1} for $\text{Mn}_2\text{Mg}_2\text{Se}_5$ (See Table 2). These values are higher than that of CrCl_3 (60.7 N m^{-1}) and CrI_3 (40.5 N m^{-1}),^[60] showing the relatively high stiffness in $\text{Mn}_2\text{Mg}_2\text{X}_5$ compounds. The smaller Y_{2D} value in $\text{Mn}_2\text{Mg}_2\text{Se}_5$ can be attributed to the weaker bonds in this crystal compared to the $\text{Mn}_2\text{Mg}_2\text{S}_5$. Poisson ratio (ν) indicates expansion or contraction perpendicular to a loading direction. The Poisson's ratios in both structures are the same ($\nu = 0.35$) and close to that of nominal 0.33 in bulk systems. This shows that straining the monolayers of $\text{Mn}_2\text{Mg}_2\text{X}_5$ along the x axis results in a shrinkage along the perpendicular y axis. We further calculated the stress-strain response of the $\text{Mn}_2\text{Mg}_2\text{X}_5$ monolayers under biaxial strain, and the results are demonstrated in Figure S5 (Supporting Information). First, it can be noted that the linear relationship between the stress and strain is maintained up to 10% strain, suggesting that these compounds remain in an elastic regime even when heavily strained. Second, failure occurs in both compounds at the UTS = 14% under biaxial strain. Strain

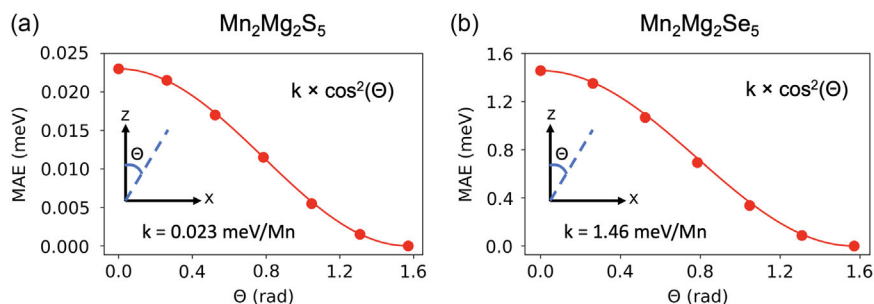


Figure 4. Angular dependence of the MAE of a) $\text{Mn}_2\text{Mg}_2\text{S}_5$ and b) $\text{Mn}_2\text{Mg}_2\text{Se}_5$ structures, k is the anisotropy constant and Θ is the polar angle of rotation, as illustrated in the insets.

engineering is a conventional method to tune the electronic and magnetic properties of 2D materials, which requires a high UTS value to prevent crystal failure. Having a UTS value of 14% renders the $\text{Mn}_2\text{Mg}_2\text{X}_5$ monolayers as suitable candidates for strain engineering.

7. Electronic Properties

The electronic properties of the $\text{Mn}_2\text{Mg}_2\text{X}_5$ monolayers are shown in Figure 5 and S6 (Supporting Information). The total density of states (DOS) plots are represented in the upper panels of Figure 5, where the blue (red) shaded area indicates the spin-up (down) channels. Spin-up is the spin-majority channel in both systems. Moreover, it can be noted that the spin-up channel is populated at the Fermi level (E_f) while spin-down has a gap of 2.13 and 2.10 eV in $\text{Mn}_2\text{Mg}_2\text{S}_5$ and $\text{Mn}_2\text{Mg}_2\text{Se}_5$ monolayers, respectively. As a result, these compounds have a half-metallic electronic nature, making them ideal for use as spin filters in future spintronics devices. The atom-projected density of states (pDOS) plots are given in the middle panels of Figure 5. It can be

noted that the pDOS of Mg atoms is negligible within -5 – 4 eV energy range. Around E_f , chalcogen's spin-up states are dominant, while Mn spin-up states are also present. It suggests that the Mn and chalcogen states are hybridized, as it was also reflected in the orbital-decomposed exchange interactions. Moreover, the Mn up-spin states are mainly populated below E_f , from around -5 to -3 eV, and the Mn down-spin states are mainly present above E_f , around 2 – 4 eV. The orbital-projected DOS for Mn atoms are demonstrated in Figure S6, Supporting Information (upper panels). The absence of any degeneracy among the d orbitals states of Mn atoms is indicative that the crystal field in these systems is not symmetric. In other words, although Mn atoms occupy a tetrahedral site, the asymmetry of the S (Se) atoms breaks the conventional t_2 and e degeneracies in a tetrahedral crystal field and lifts them all. The lower panels of Figure 5 depict the spin-polarized band structures of $\text{Mn}_2\text{Mg}_2\text{X}_5$ monolayers. Resonant with the half-metallic nature of the compounds, only spin-up bands cross the Fermi level. It can be noted that the valence band maximum (VBM) for both spin channels lies at the Γ point. The conduction band minimum, however, is located at the M point for spin-up and K point for spin-down

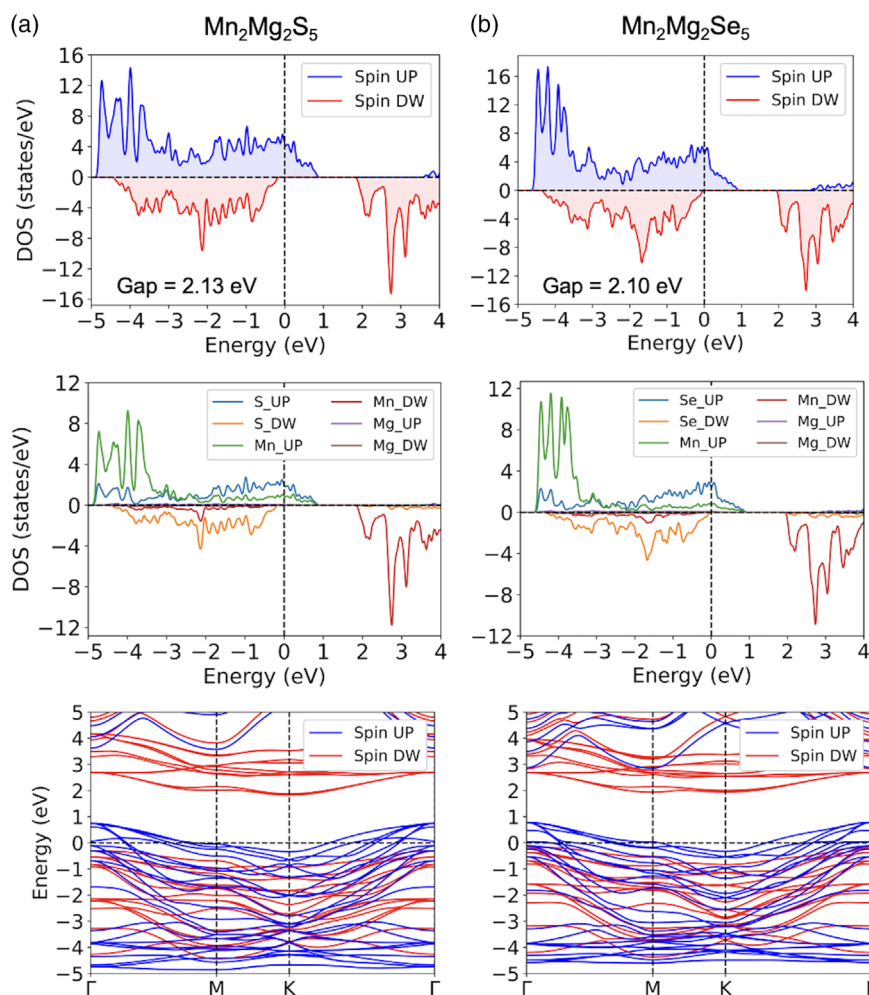


Figure 5. Density of states (DOS) (upper panels), atom-projected DOS (middle panels), and spin-polarized electronic band structures (lower panels) for a) $\text{Mn}_2\text{Mg}_2\text{S}_5$ and b) $\text{Mn}_2\text{Mg}_2\text{Se}_5$ structures.

channel. Having an indirect spin-down bandgap suggests that only phonon-mediated excitation can be predicted in this channel. The orbital-projected band structures (fat-bands), accentuating the contribution of Mn d-states, are visualized in the lower panels of Figure S6 (Supporting Information), where the size of circles is proportional to the projection of d-states at each segment of the BZ. While d-states are dominant in the conduction bands, in the valence bands close to the Fermi level, d-states are less active. However, in these bands, around the VBM, at the Γ point, the presence of d-states is stronger than other high-symmetry points. Lastly, we investigated the effects of strain engineering on the band structure of these compounds, where a biaxial strain between -4% and 10% was applied to the $\text{Mn}_2\text{Mg}_2\text{X}_5$ monolayers. The results are presented in Figure S7 (Supporting Information). The overall electronic properties, including the half-metallicity, were found to be independent of the size of strain, as the spin-down gap remains open and retains its $E_g = 2$ eV. Moreover, it was found that a compressive strain tends to decrease the size of this gap while a tensile strain widens the gap.

8. MC Simulations

Magnetic order in 2D magnets is less robust against thermal fluctuations than that of the bulk crystals. Therefore, it is necessary to have an estimation of the magnetic transition temperature (T_C) in these 2D systems. Accordingly, at first, we estimated the mean-field Curie temperature ($T_{C\text{-MF}}$) based on the following expression:

$$T_c = \frac{zJ}{2k_B} \quad (5)$$

where z is the coordination number, J is the coupling constant, and k_B is the Boltzmann constant. We found $T_{C\text{-MF}} = 316$ and 276 K for $\text{Mn}_2\text{Mg}_2\text{S}_5$ and $\text{Mn}_2\text{Mg}_2\text{Se}_5$, respectively, as reported in Table 3. However, it is known that mean-field estimation generally overestimates the T_C . Thus, we further performed classical MC simulations of temperature-dependent magnetic properties, considering localized spin moments, based on the following Heisenberg spin Hamiltonian:

$$H = - \sum_{i,j} J_{ij} \vec{S}_i \cdot \vec{S}_j - \sum_i K_i (S_i^z)^2 \quad (6)$$

where J_{ij} is the isotropic symmetric exchange interactions between i th and j th sites, K_i is the single-ion anisotropy, and \vec{S}_i and \vec{S}_j are spin vectors. The upper panel of Figure S9 (Supporting Information) shows normalized magnetization (M) versus temperature and the lower panel shows the heat capacity versus temperature for $\text{Mn}_2\text{Mg}_2\text{S}_5$ and $\text{Mn}_2\text{Mg}_2\text{Se}_5$. An accurate estimation of the transition temperature ($T_{C\text{-MF}}$) can be achieved from the evolution of heat capacity versus temperature, where the sharp peak corresponds to $T_{C\text{-MF}}$. Accordingly, the transition from an ordered FM to a paramagnetic phase occurs at $T_{C\text{-MF}} = 205$ and 193 K for $\text{Mn}_2\text{Mg}_2\text{S}_5$ and $\text{Mn}_2\text{Mg}_2\text{Se}_5$, respectively. Generally, stronger J_{ij} interactions and stronger MAE contribute to higher T_C . Here, the weaker J_{ij}

interactions in $\text{Mn}_2\text{Mg}_2\text{Se}_5$ is compensated with stronger MAE found in this compound to bring the T_C close to that of $\text{Mn}_2\text{Mg}_2\text{S}_5$. Although the T_C in these compounds are below room temperature, they are still higher than that of most of the synthesized 2D magnets such as semiconducting CrI_3 ($T_C \approx 45$ K^[8]) or metallic Fe_3GeTe_2 ($T_C \approx 130$ K^[13]).

9. Conclusion

The structural, magnetic, mechanical, and electronic properties of $\text{Mn}_2\text{Mg}_2\text{X}_5$ ($X = \text{S}, \text{Se}$) monolayers were systematically studied using first-principles methods. We analyzed and verified the energetic, dynamical, thermal, and mechanical stability of these compounds. A FM ground state was found for these materials, further confirmed by the calculation of Heisenberg exchange interactions. An indirect exchange, mediated by $d_{z^2}-p_z$ interactions between Mn and chalcogen atoms, was proposed as the main exchange mechanism, using orbital decomposed exchange interactions and tight-binding hopping parameters. It was found that these 2D materials offer a half-metallic nature with a bandgap of ≈ 2 eV in their spin-down channel, rendering them suitable candidates for spin-filtering applications. A UTS of 14% was calculated for both compounds. According to MC simulations, the transition temperature of these monolayers is approximately 200 K, higher than that of synthesized 2D magnets.

Supporting Information

Supporting Information is available from the Wiley Online Library or from the author.

Acknowledgements

B.S. acknowledges financial support from Swedish Research Council (grant no. 2022-04309) and Carl Tryggers Stiftelse (CTS, grant no. 20:378). The computations were enabled by resources provided by the National Academic Infrastructure for Supercomputing in Sweden (NAISS) at UPPMAX (NAISS, grant no. 2023/5-238) and the Swedish National Infrastructure for Computing (SNIC) (SNIC, grant no. 2022/3-30) at NSC and PDC partially funded by the Swedish Research Council through grant agreement nos. 2022-06725 and 2018-05973. B.S. and S. E. also acknowledge the allocation of supercomputing hours in EuroHPC resources in Karolina supercomputer (grant nos. EU2022D10-059 and EU2022D11-001) in the Czech Republic and LUMI supercomputer (grant nos. EHPC-DEV-2022D10-059 and EHPC-DEV-2022D10-057) in Finland.

Conflict of Interest

The authors declare no conflict of interest.

Data Availability Statement

The data that support the findings of this study are available from the corresponding author upon reasonable request.

Keywords

Curie temperature, density-functional theory, ferromagnetic 2D materials, half-metallic, magnetic anisotropy

Received: November 1, 2023

Published online: December 6, 2023

- [1] N. D. Mermin, H. Wagner, *Phys. Rev. Lett.* **1966**, 17, 1133.
- [2] K.-Z. Du, X.-Z. Wang, Y. Liu, P. Hu, M. I. B. Utama, C. K. Gan, Q. Xiong, C. Kloc, *ACS Nano* **2016**, 10, 1738.
- [3] J.-U. Lee, S. Lee, J. H. Ryoo, S. Kang, T. Y. Kim, P. Kim, C.-H. Park, J.-G. Park, H. Cheong, *Nano Lett.* **2016**, 16, 7433.
- [4] G. Le Flem, J. Soubeyroux, C. Delmas, *J. Magn. Magn. Mater.* **1980**, 15, 1315.
- [5] M. Bander, D. Mills, *Phys. Rev. B* **1988**, 38, 12015.
- [6] Y. Ma, Y. Dai, M. Guo, C. Niu, Y. Zhu, B. Huang, *ACS Nano* **2012**, 6, 1695.
- [7] C. Gong, L. Li, Z. Li, H. Ji, A. Stern, Y. Xia, T. Cao, W. Bao, C. Wang, Y. Wang, Z. Q. Qiu, R. J. Cava, S. G. Louie, J. Xia, X. Zhang, *Nature* **2017**, 546, 265.
- [8] B. Huang, G. Clark, E. Navarro-Moratalla, D. R. Klein, R. Cheng, K. L. Seyler, D. Zhong, E. Schmidgall, M. A. McGuire, D. H. Cobden, W. Yao, D. Xiao, P. Jarillo-Herrero, X. Xu, *Nature* **2017**, 546, 270.
- [9] A. F. May, D. Ovchinnikov, Q. Zheng, R. Hermann, S. Calder, B. Huang, Z. Fei, Y. Liu, X. Xu, M. A. McGuire, *ACS Nano* **2019**, 13, 4436.
- [10] S. Ershadrad, S. Ghosh, D. Wang, Y. Kvashnin, B. Sanyal, *J. Phys. Chem. Lett.* **2022**, 13, 4877.
- [11] S. Ghosh, S. Ershadrad, V. Borisov, B. Sanyal, *npj Comput. Mater.* **2023**, 9, 86.
- [12] S. Ghosh, S. Ershadrad, B. Sanyal, arXiv:2305.04366, **2023**.
- [13] Z. Fei, B. Huang, P. Malinowski, W. Wang, T. Song, J. Sanchez, W. Yao, D. Xiao, X. Zhu, A. F. May, W. Wu, D. H. Cobden, J.-H. Chu, X. Xu, *Nat. Mater.* **2018**, 17, 778.
- [14] R. De Groot, F. Mueller, P. V. van Engen, K. Buschow, *Phys. Rev. Lett.* **1983**, 50, 2024.
- [15] I. Galanakis, *Phys. Rev. B* **2002**, 66, 012406.
- [16] W. E. Pickett, *Phys. Rev. B* **1998**, 57, 10613.
- [17] J. Park, S. Kwon, B. Min, *Phys. Rev. B* **2002**, 65, 174401.
- [18] X. Wu, L. Hu, D. Gu, G. Gao, *J. Phys. Chem. C* **2021**, 125, 6341.
- [19] W. Alfalasi, Y. P. Feng, N. Tit, *Acta Mater.* **2023**, 246, 118655.
- [20] X. Wu, L. Xiong, Y. Feng, C. Wang, G. Gao, *Chem. Phys.* **2019**, 150, 6.
- [21] H. Wang, J. Zhang, X. Hang, X. Zhang, J. Xie, B. Pan, Y. Xie, *Angew. Chem.* **2015**, 127, 1211.
- [22] B. Wang, Y. Zhang, L. Ma, Q. Wu, Y. Guo, X. Zhang, J. Wang, *Nanoscale* **2019**, 11, 4204.
- [23] H. Zeng, S. Jin, J. Wang, Y. Hu, X. Fan, *J. Mater. Sci.* **2021**, 56, 13215.
- [24] G. Xiao, W.-Z. Xiao, Y.-X. Feng, Q.-Y. Rong, Q. Chen, *Nanoscale* **2023**, 15, 17963.
- [25] B. Abyaz, Z. Mahdavi, G. Schreckenbach, *Appl. Surf. Sci.* **2023**, 621, 156892.
- [26] V. Wang, G. Tang, Y.-C. Liu, R.-T. Wang, H. Mizuseki, Y. Kawazoe, J. Nara, W. T. Geng, *J. Phys. Chem. Lett.* **2022**, 13, 11581.
- [27] J. Kim, J. Kim, S.-H. Jhi, *Phys. Rev. B* **2010**, 82, 201312.
- [28] I. V. Silkin, Y. M. Koroteev, S. V. Eremeev, G. Bihlmayer, E. V. Chulkov, *JETP Lett.* **2011**, 94, 217.
- [29] S. Nakatsuji, H. Tonomura, K. Onuma, Y. Nambu, O. Sakai, Y. Maeno, R. T. Macaluso, J. Y. Chan, *Phys. Rev. Lett.* **2007**, 99, 157203.
- [30] K. Takubo, T. Mizokawa, Y. Nambu, S. Nakatsuji, *Phys. Rev. B* **2009**, 79, 134422.
- [31] J. Shen, X. Xu, M. He, Y. Liu, Y. Han, Z. Qu, *Chin. Phys. B* **2022**, 31, 067105.
- [32] W. Kohn, L. J. Sham, *Phys. Rev.* **1965**, 140, A1133.
- [33] P. Hohenberg, W. Kohn, *Phys. Rev.* **1964**, 136, B864.
- [34] G. Kresse, J. Hafner, *Phys. Rev. B* **1993**, 47, 558.
- [35] G. Kresse, J. Hafner, *Phys. Rev. B* **1994**, 49, 14251.
- [36] G. Kresse, J. Furthmüller, *Comput. Mater. Sci.* **1996**, 6, 15.
- [37] G. Kresse, J. Furthmüller, *Phys. Rev. B* **1996**, 54, 11169.
- [38] J. P. Perdew, K. Burke, M. Ernzerhof, *Phys. Rev. Lett.* **1996**, 77, 3865.
- [39] P. E. Blöchl, *Phys. Rev. B* **1994**, 50, 17953.
- [40] E. Şaşoğlu, C. Friedrich, S. Blügel, *Phys. Rev. B* **2011**, 83, 121101.
- [41] J. Hong, A. Stroppa, J. Íñiguez, S. Picozzi, D. Vanderbilt, *Phys. Rev. B* **2012**, 85, 054417.
- [42] A. K. Aghaee, S. Belbasi, H. Hadipour, *Phys. Rev. B* **2022**, 105, 115115.
- [43] G. Henkelman, A. Arnaldsson, H. Jónsson, *Comput. Mater. Sci.* **2006**, 36, 354.
- [44] A. Togo, I. Tanaka, *Scr. Mater.* **2015**, 108, 1.
- [45] A. A. Mostofi, J. R. Yates, Y.-S. Lee, I. Souza, D. Vanderbilt, N. Marzari, *Comput. Phys. Commun.* **2008**, 178, 685.
- [46] X. He, N. Helbig, M. J. Verstraete, E. Bousquet, *Comput. Phys. Commun.* **2021**, 264, 107938.
- [47] A. I. Liechtenstein, M. Katsnelson, V. Antropov, V. Gubanov, *J. Magn. Magn. Mater.* **1987**, 67, 65.
- [48] O. Eriksson, A. Bergman, L. Bergqvist, J. Hellsvik, *Atomistic Spin Dynamics: Foundations and Applications*, Oxford University Press, Oxford, UK **2017**.
- [49] J. K. Burdett, T. A. McCormick, *J. Phys. Chem. A* **1998**, 102, 6366.
- [50] A. Jain, S. P. Ong, G. Hautier, W. Chen, W. D. Richards, S. Dacek, S. Cholia, D. Gunter, D. Skinner, G. Ceder, K. A. Persson, *APL Mater.* **2013**, 1, 011002.
- [51] V. Vierimaa, A. V. Krashennnikov, H.-P. Komsa, *Nanoscale* **2016**, 8, 7949.
- [52] S. Cahangirov, M. Topsakal, E. Aktürk, H. Şahin, S. Ciraci, *Phys. Rev. Lett.* **2009**, 102, 236804.
- [53] Y. Chen, G. Wang, H. Yuan, H. Chen, *Phys. Status Solidi B* **2022**, 259, 2100443.
- [54] M. A. McGuire, H. Dixit, V. R. Cooper, B. C. Sales, *Chem. Mater.* **2015**, 27, 612.
- [55] Q. Liu, J. Xing, Z. Jiang, Y. Guo, X. Jiang, Y. Qi, J. Zhao, *Commun. Phys.* **2022**, 5, 140.
- [56] M. Born, K. Huang, *Dynamical Theory of Crystal Lattices*, Clarendon Press, Clarendon, Oxford **1954**.
- [57] F. Mouhat, F.-X. Coudert, *Phys. Rev. B* **2014**, 90, 224104.
- [58] L. Webster, J.-A. Yan, *Phys. Rev. B* **2018**, 98, 144411.
- [59] K. Wang, T. Hu, F. Jia, G. Zhao, Y. Liu, I. V. Solov'yev, A. P. Pyatakov, A. K. Zvezdin, W. Ren, *Appl. Phys. Lett.* **2019**, 114, 9.
- [60] F. Cantos-Prieto, A. Falin, M. Alliat, D. Qian, R. Zhang, T. Tao, M. R. Barnett, E. J. Santos, L. H. Li, E. Navarro-Moratalla, *Nano Lett.* **2021**, 21, 3379.